PAPER

Check for updates

Preparation and photoelectrochemical properties of BiFeO₃/BiOI composites

Yuxuan Lei, [ID] [a] Yaping Zhang,*[a] Wenming Ding,[b] Lianqing Yu, [ID] *[b] Xinpeng Zhou[a] and Chi-Man Lawrence Wu [ID] [c]

BiFeO₃ thin films were spin coated onto FTO. BiFeO₃/BiOI composites have been successfully synthesized by an electrochemical deposition method. The morphology, structure and optical absorption properties of the as-synthesized samples were characterized *via* XRD, SEM, and UV-Vis DRS. The effect of the BiOI electrodeposition cycles on the photoelectrochemical properties of the BiFeO₃/BiOI composites were investigated. The results showed that the photoelectrochemical properties were enhanced under simulated solar light. The composite could achieve an optimum photocurrent density of 16.03 μA cm^{-2} at 0 V (*vs.* Ag/AgCl), which is more than twice that of pure BiFeO₃ thin films (6.3 μA cm^{-2}). In addition, the Mott–Schottky curves indicate an improvement in the carrier density of the composite. The enhanced photoelectrochemical properties of the composites can be attributed to the formation of a heterojunction at the interface and the band bending of the ferroelectric material BiFeO₃.

1. Introduction

Recently, perovskite BiFeO₃ (BFO) has received great attention due to its narrow band gap (2.1–2.7 eV), good chemical stability and low cost.[1–3] As a typical representative of ferroelectric materials, the internal electric field induced by self-polarization can facilitate the separation of photogenerated electrons and holes, since the special electric field modulates the chemical potential and surface band bending, which play a crucial role in improving the photoelectrochemical (PEC) properties.[4–6] However, the PEC activities of BFO are still unsatisfactory because of its poor charge transport properties and electron–hole recombination.[7–9] Based on this situation, many strategies have been proposed to obtain better PEC performances of BFO. Wang *et al.*[3] adapted a BFO thin film with a cobalt-phosphate cocatalyst by a photoassisted electrodeposition method, obtaining a photocurrent density nearly 8 times that of the bare BFO electrode. Baqiah *et al.*[4] introduced Fe₃O₄ into the BFO matrix to improve the photocurrent performance by narrowing the band gap and reducing the recombination of electron holes. Bera *et al.*[5] decorated BFO nanosheets with Au, and the surface-plasmon effect (SPR) of Au nanoparticles benefited the generation of photoelectrons and holes. As a result, the optimum photocurrent density of the decorated composite increased 4-fold to 2.14 μA cm^{-2} (0.6 V *vs.* Ag/AgCl).

In research on efficient and stable photocatalyst materials, BiOI has become a research hotpot because of its small band gap (1.72–1.92 eV) and unique layered tetragonal structure. The special layered structure containing $[Bi_2O_2]^{2+}$ slabs is interleaved by double slabs of halogen atoms, and the weak inter-layer van der Waals interaction and strong interlayer bonding lead to excellent PEC properties.[10,11] Accordingly, BiOI can be used to construct a heterojunction structure to improve the PEC properties of materials.[12–15] For example, Liu *et al.*[13] constructed a BiOI/BiPO₄ p–n heterojunction structure *via* two-step electrodeposition and obtained an enhanced photocurrent density of 2.5 μA cm^{-2}, which is twice that of bare BiOI and nearly 20 times higher than that of pure BiPO₄. Ye *et al.*[15] employed BiOI to decorate ZnO/CdS nanorod arrays to overcome the problem of photocorrosion, and consequently, a long-term stability over 6000 s and a high photocurrent density of 3.04 mA cm^{-2} (1.75 times that of the ZnO/CdS photoanode) were achieved. Thus, the p–n junction formed between CdS and BiOI could be responsible for enhancing the PEC properties.

Considering the abovementioned unique characteristics of BFO and BiOI, we are curious about the synergistic effect between the spontaneous polarization property of BFO and the peculiar layered structure of BiOI. Malathi *et al.*[16] attempted to fabricate BFO/BiOI composite particles for the photo-degradation of RhB but achieved only a low photocurrent density of 0.06 μA cm^{-2}, exhibiting a negligible improvement of 0.02 μA cm^{-2} over BiFeO₃. In this work, BiOI-decorated BFO thin films were prepared by chemical solution deposition and electrodeposition. The photocurrent density of the decorated samples, 16.03 μA cm^{-2}, was more than 2 times larger than that of pure BiFeO₃, 6.3 μA cm^{-2}.

[a] *College of Science, China University of Petroleum (East China), Qingdao, 266580, P. R. China. E-mail: zhangyp@upc.edu.cn*

[b] *College of Materials Science and Engineering, China University of Petroleum (East China), Qingdao, 266580, P. R. China. E-mail: iyy2000@163.com*

[c] *Department of Materials Science and Engineering, City University of Hong Kong, Hong Kong, SAR, P. R. China*

2. Experimental section

2.1 Sample preparation

$BiFeO_3$ thin films were synthesized *via* a chemical solution deposition method, as reported previously.[17] Typically, 0.85 g of $Bi(NO_3)_3$, 0.8 g of $Fe(NO_3)_3$ and 3.36 g of citric acid were dissolved into 4.0 g of ethylene glycol by heating at 90 ($\pm$3) °C and stirring for 3 h to form a sol–gel. The sol–gel was spin coated onto FTO at 2300 rpm for 60 s to obtain amorphous $BiFeO_3$ films and then crystallized by annealing at 500 °C for 30 min in a tube furnace. The obtained $BiFeO_3$ thin films were denoted by BFO. The BiOI films were prepared *via* the electrodeposition method under a three-electrode system.[18] The obtained BFO electrode, Pt wire and Ag/AgCl electrode were used as the working, counter and reference electrodes, respectively. To obtain 0.04 M $Bi(NO_3)_3$ as the electrolyte, $Bi(NO_3)_3$ was dissolved in 100 mL of a 0.4 M KI solution. The pH was adjusted to 1.7 with HNO_3, and the $Bi(NO_3)_3$ solution was mixed with 40 mL of absolute ethanol containing 0.23 M *p*-benzoquinone and vigorously stirred for 30 min. Electrodeposition was performed in the abovementioned mixed solution at −0.1 V for 6–12 min, and the as-prepared samples were denoted by BFO/BI-*n* (n = 6, 8, 10, 12). The experimental progress is shown in Scheme 1.

2.2 Characterization

The crystal structures of the samples were identified by a Dmax-2700 X-ray diffractometer (XRD). The surface morphology was observed using a Hitachi S-4800 field-emission scanning electron microscope (SEM). Transmission electron microscopy (TEM) images were taken with a JEOL JEM-2100 transmission electron microscope. The optical absorption properties were measured with a U-3900 UV-Vis diffuse reflectance spectrometer (DRS), with wavelengths ranging from 280 to 790 nm. The photoluminescence (PL) spectra were obtained using a Hitachi F-7000 fluorescence spectrophotometer. The Fourier transform infrared (FT-IR) spectra were performed *via* a Bruker Tensor II spectrometer in the wavenumber varying from 4000 to 400 cm^{-1}.

The photoelectrochemical (PEC) performance of the samples was investigated by a CHI 760E electrochemical workstation under AM1.5G illumination (I_0 = 100 mW cm^{-2}, the wavelength range was 380–780 nm). In a classical three-electrode system,
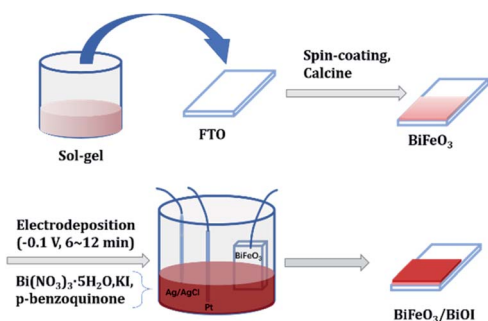
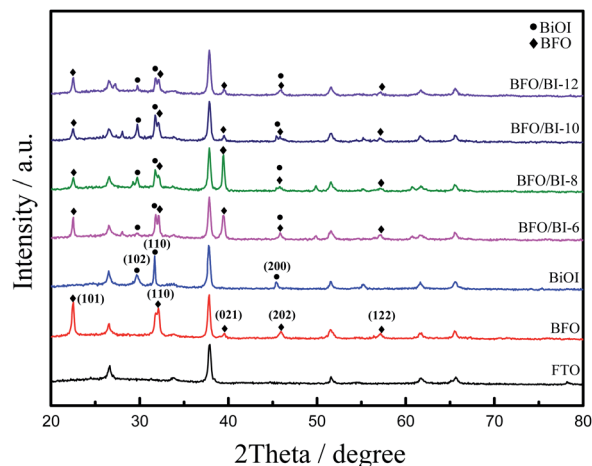Scheme 1   Diagram of the BFO/BI-*n* sample preparation process.

Fig. 1   XRD patterns of pure BFO, BiOI and BFO/BI-*n*.

the as-synthesized photoanodes, Pt wire and Ag/AgCl were employed as the working, counter and reference electrodes, respectively. A 1 M Na_2SO_3 aqueous solution was used as the electrolyte. The photocurrent response plots (*I–t* plot) were obtained at a 0 V (*vs.* Ag/AgCl) potential bias under intermittent illumination. The linear scanning voltammetry (LSV) curves were acquired at a scanning rate of 1 mV s^{-1}, and the Mott–Schottky plots were recorded from −0.6 V to 0.6 V (*vs.* Ag/AgCl) at an applied frequency of 5 kHz.

3. Results and discussion

3.1 Characterization of phase and morphology

The XRD patterns of BiOI, BFO and BFO/BI-*n* are presented in Fig. 1. For BFO, the pattern indicates that the polycrystalline BFO thin film with a perovskite structure is free from a secondary phase.[19] Three main peaks are observed at 2θ = 22.51°, 32.11° and 45.97°, which could be attributed to the (101), (110), and (202) facets of the $BiFeO_3$ perovskite structure (PDF #20-0169), respectively. For BiOI, peaks arise at 2θ = 29.66°, 31.69° and 45.41°, corresponding to the (102), (110) and (200) facets of BiOI (PDF #10-0445), respectively. All the diffraction peaks of the composites can be indexed as $BiFeO_3$ and BiOI, indicating that the composite sample consists of BFO and BiOI, which confirms the successful formation of the heterojunction.[20] The intensity of the diffraction peak corresponding to the (110) facet of pure BiOI decreases in the BFO/BI-*n* (n = 6, 8, 10, and 12) samples, which may be due to the contribution of $BiFeO_3$ to the reorientation of the BiOI crystal growth.[21]

Fig. 2 shows the SEM and TEM images of pure BiOI and the BFO/BI-10 composite. The pure electrodeposited BiOI film is composed of a thin two-dimensional plate-like crystal with a length of more than 2 μm, and the special morphology of BiOI, which has a larger specific surface area, favors the combination of BiOI and BFO. No obvious structural changes were observed after BFO and BiOI combined, as illustrated in Fig. 2(b). BFO is cottony when coupled with plate-like BiOI. Moreover, the

presence of Bi, O, Fe, and I in the EDS maps (Fig. 2(c–f)) could further confirm the successful fabrication of the $BiFeO_3$/BiOI composite. According to the TEM images of the BFO/BI composite (Fig. 2(g and h)), no core–shell structure was observed.

3.2 FT-IR analysis

Fig. 3 shows the FT-IR spectra of the pure BFO, BiOI and BFO/BI-10 samples. For pristine BiOI, the band observed at 494 cm^{-1} can be credited to the symmetrical A_{2u}-type vibration mode of the Bi–O bond.[22] In the FT-IR spectrum of pure BFO, the band situated at 553 cm^{-1} is credited to the Fe–O stretching and bending vibrations.[23] The bands at 1620 cm^{-1} and 3411 cm^{-1} in the spectrum of pristine BiOI and BFO are attributed to the ν(O–H) stretching and δ(O–H) bending vibrations of the hydroxyl groups. Note that the intensity of the peaks situated at 3411 cm^{-1} and 1620 cm^{-1} decreases in BFO/BI-10, which indicates the co-existence of BFO and BiOI.[16] Moreover, the characteristic peak of BFO positioned at 553 cm^{-1} shifts
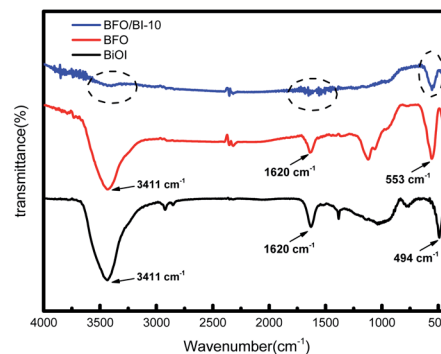

Fig. 3 FT-IR spectra of BiOI, BFO and BFO/BI-10.

after BFO combines with BiOI, which suggested the formation of a heterojunction between BFO and BiOI.[24]

3.3 Optical absorption properties

The absorption of the synthesized BFO, BiOI and BFO/BI-n thin films was investigated by UV-Vis DRS analysis, as shown in Fig. 4. The composites exhibit better visible region absorption than pristine BFO and BiOI. The band gap energy of the prepared materials was evaluated by the tangent intercept of the plotted linear part,[24] and the measured band gaps of pure BFO, BiOI, and BFO/BI-10 were found to be 1.84 eV, 1.93 eV, and 1.81 eV, respectively. The composition of BFO and BiOI extends the range of light absorption and decreases the band gap energy, which assists in the generation of photoelectrons and holes while suppressing the recombination of the photo-generated carriers.[25,26]

3.4 Photoelectrochemical properties of BFO/BI-n

Fig. 5(a) shows the I–t plots of the samples obtained at a 0 V bias voltage (*vs.* Ag/AgCl). Upon simulated one sun illumination, the transient photocurrent of all the composited samples was better than that of the pristine samples. The photocurrent density of BFO/BI-n first increased and then decreased as the number of electrodeposition cycles of BiOI increased, in which BFO/BI-10 reached the highest photocurrent density of 16.03 $\mu A\ cm^{-2}$, which was over twice as high as that of bare BFO (6.3 $\mu A\ cm^{-2}$)
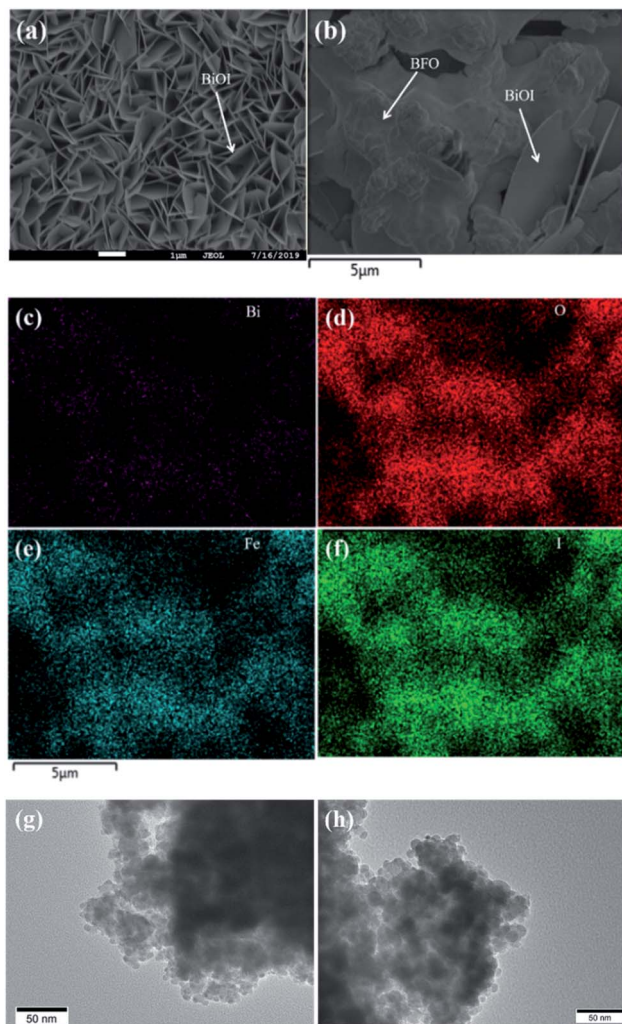

Fig. 2 SEM images of (a) pure BiOI and (b) the BiOI/BI composite. (c–f) EDS elemental maps of Bi, O, Fe, and I. (g and h) TEM images of BiOI/BI composite.
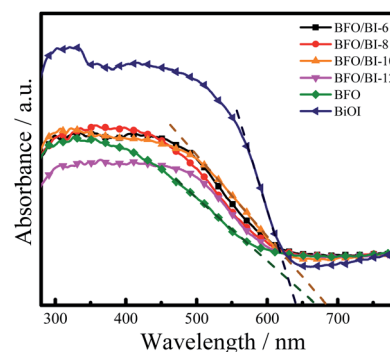

Fig. 4 UV-Vis diffuse reflectance spectra of the BFO, BiOI and BFO/BI-n samples.

and much higher than that of pure BiOI (1.8 μA cm⁻²). Introducing BiOI composites on the BFO thin films results in the formation of a heterojunction in the interface between BFO and

Fig. 5 (a) *I*–*t* curves, (b) LSV, (c) Mott−Schottky curves, (d) PL spectra of BFO, BiOI and BFO/BI-*n*.

BiOI, which benefits the separation of the photogenerated electrons and holes due to the improvement in the lifetime period of the photoinduced carriers,[16,25] thus improving the photocurrent density. However, overdeposition of BiOI will shield BFO layer absorption from light,[27,28] resulting in the low photocurrent density of BFO/BI-12.

Fig. 5(b) presents the LSV plots of the as-synthesized samples. The current density of the BFO/BI-*n* composite was greatly improved across the entire potential range than that of the BFO thin film photoanode. The BFO/BI-10 sample exhibits the best PEC property, with a photocurrent density of 1.658 mA cm⁻² at 0.6 V (*vs.* Ag/AgCl), which is much higher than that of bare BFO (0.102 mA cm⁻²). The enhancement in the PEC properties could be ascribed to the band bending resulting from the self-polarization of the ferroelectric material BFO, which facilitates the transport of photogenerated electrons and holes.[29–31]

The Mott–Schottky curve can be used to index the density of charge carriers in semiconductors.[28,32] In the PEC system, the amplifier photovoltage excited by light charges the space-charge capacitance of the semiconductor, thus influencing the charge carrier density (*N*ₐ), which can be expressed as

$$N_{\mathrm{D}} = \frac{2}{e\varepsilon\varepsilon_0 m}$$

where *e* is the elementary electron charge, *ε* is the dielectric constant, *ε*₀ is the permittivity in a vacuum ($\varepsilon_0 = 8.85 \times 10^{-14}$ F cm⁻¹), and *m* is the slope of the Mott–Schottky curves.[3] Obviously, a semiconductor with a larger carrier density corresponds to a Mott–Schottky curve with a smaller slope. Fig. 5(c) shows the Mott–Schottky curves of the samples. The slopes of the Mott–Schottky curves of all the composite samples are smaller than those of BFO and BiOI, meaning that the carrier density of the composite is higher than that of the pristine samples. In addition, BFO/BI-10 has the highest carrier density among the samples, which is consistent with the *I*–*t* plots. The improvement in the carrier could be attributed to two factors.[33] First, the coupling of the two semiconductors reduces the band gap, thus improving light absorption and the generation of photoelectrons and holes. Second, the formation of the heterojunction is conducive to the separation of the photoelectrons and holes, which inhibits the recombination of the photogenerated carriers and therefore prolongs the life span of carriers. Additionally, the flat band potentials of BFO and BiOI, calculated from the horizontal axis intercepts of the linear region of the Mott–Schottky plots,[3,34] are found to be −0.25 V and −0.5 V (*vs.* Ag/AgCl), respectively.

PL spectra can be adapted to investigate the charge recombination progress of materials.[35,36] As shown in Fig. 5(d), the PL intensity of BFO/BI-10 was lower than that of the BFO and BiOI photoanodes, indicating that the recombination rate of the photogenerated electrons and holes in the BFO/BI-10 photoanode is lower than that in the BFO and BiOI photoanodes, which contributes to the improvement of PEC performance. The results of the PL spectral analysis confirm the explanation for the improvement in the photocurrent density.
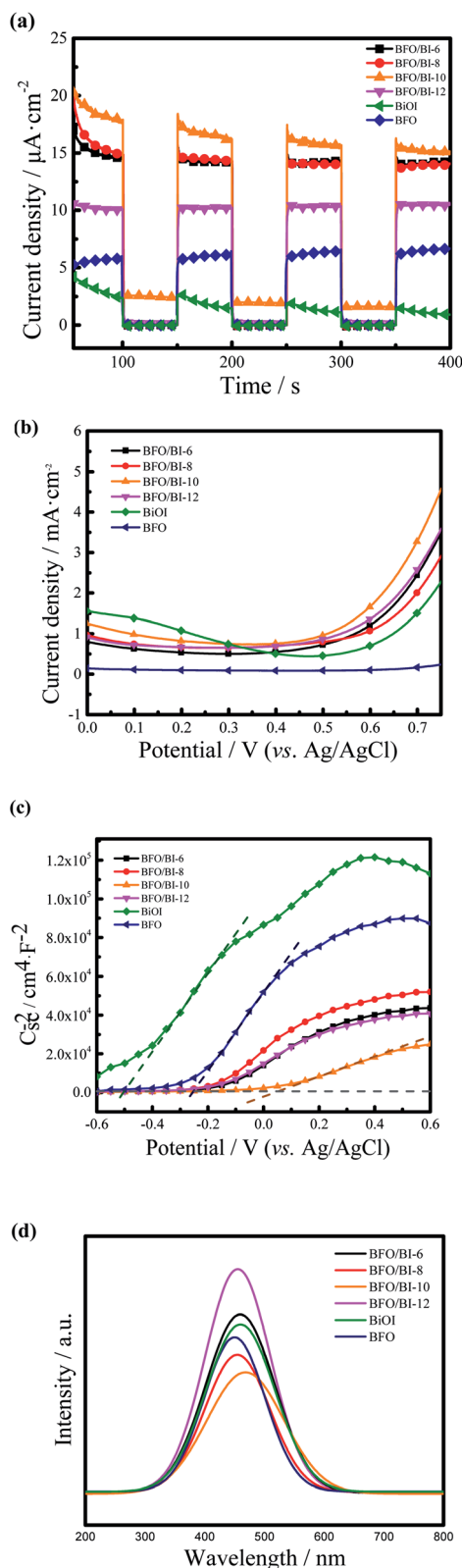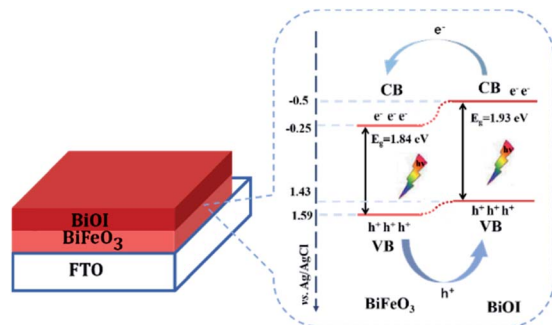
Fig. 6 Energy band schematic diagram of BFO/BI.

4. Mechanistic analysis

The energy bands of the BFO/BI composite were proposed, as illustrated in Fig. 6. During the process of generating and transporting the photoelectrons and holes in the hetero-junction, three main steps are included: first, light is absorbed by the semiconductor, where the coupling of two semi-conductors narrows the bandgap, thus increasing light absorption and generating more photoelectron–hole pairs; second, the photoelectrons generated would transfer to the conduction band (CB) from the valence band (VB), and the holes would stay in the VB; and third, since the CB and VB positions of BiOI are higher than those of BFO, the photoelectrons in the CB of BiOI would further transfer to the CB of BFO; furthermore, the holes in the VB of BFO would move to the VB of BiOI, and as a result of this transition, the photogenerated carriers were efficiently separated. Furthermore, the band bending at the interface between BFO and BiOI, which was induced by the spontaneous polarization of BFO, could accelerate carrier transfer,[31,37,38] thus improving the separation efficiency of photoelectrons and holes and extending the lifetime of the carriers, which contributes greatly to enhancing the PEC properties of the composite.

5. Conclusions

BFO thin films were prepared *via* the chemical solution deposition method, and two-dimensional plate-like BiOI was fabricated by electrodeposition on pristine BFO thin films. The formation of heterojunctions and band bending at the interface can accelerate the transfer and suppress the recombination of photogenerated electrons and holes. The maximum photocurrent density obtained under solar light was 16.03 μA cm^{-2} for BFO/BI-10 at 0 V (*vs.* Ag/AgCl), which is more than twice as high as that of pure BFO (6.3 μA cm^{-2}). The carrier density of all the composite samples is higher than that of pristine BFO and BiOI. The BFO/BI composite, which exhibits excellent photoelectrochemical properties, demonstrates great potential in solar energy conversion applications.

Conflicts of interest

There are no conflicts to declare.

References

1 F. Haydous, N. D. Scarisoreanu, R. Birjega, V. Ion, T. Lippert, N. Dumitrescu, A. Moldovan, A. Andrei, V. S. Teodorescu, C. Ghica, R. Negrea and M. Dinescu, *Sci. Rep.*, 2018, **8**, 15826.

2 K. H. Tan, Y. W. Chen, C. N. Van, H. Wang, J. W. Chen, F. S. Lim, K. H. Chew, Q. Zhan, C. L. Wu, S. P. Chai, Y. H. Chu and W. S. Chang, *ACS Appl. Mater. Interfaces*, 2019, **11**, 1655–1664.

3 Y. Wang, D. Chen, S. Wang, J. Liang, L. Qin, X. Sun and Y. Huang, *J. Electrochem. Soc.*, 2019, **166**, D308–D314.

4 H. Baqiah, Z. A. Talib, A. H. Shaari, M. M. Dihom, M. M. A. Kechik, S. K. Chen, J. Y. C. Liew, Z. Zainal and L. Mohd Fudzi, *J. Sol-Gel Sci. Technol.*, 2019, **91**, 624–633.

5 S. Bera, S. Ghosh, S. Shyamal, C. Bhattacharya and R. N. Basu, *Sol. Energy Mater. Sol. Cells*, 2019, **194**, 195–206.

6 Y. L. Huang, W. S. Chang, C. N. Van, H. J. Liu, K. A. Tsai, J. W. Chen, H. H. Kuo, W. Y. Tzeng, Y. C. Chen, C. L. Wu, C. W. Luo, Y. J. Hsu and Y. H. Chu, *Nanoscale*, 2016, **8**, 15795–15801.

7 Q. Liu, Y. Zhou, L. You, J. Wang, M. Shen and L. Fang, *Appl. Phys. Lett.*, 2016, **108**, 022902.

8 W. Ramadan and A. Gupta, *J. Nanosci. Nanotechnol.*, 2018, **18**, 7804–7810.

9 A. K. Vishwakarma, P. Tripathi, A. Srivastava, A. S. K. Sinha and O. N. Srivastava, *Int. J. Hydrogen Energy*, 2017, **42**, 22677–22686.

10 L. Hu, Y. Liao, D. Xia, Q. Zhang, H. He, J. Yang, Y. Huang, H. Liu, F. Zhang, C. He and D. Shu, *Catal. Today*, 2020, **339**, 379–390.

11 Z. Liu, Q. Wang, X. Tan, Y. Wang, R. Jin and S. Gao, *Sep. Purif. Technol.*, 2019, **215**, 565–572.

12 M. Li, R. He, S. Wang, C. Feng, H. Wu and H. Mei, *Microchim. Acta*, 2019, **186**, 345.

13 S. Liu, M. Zhao, Z. He, Y. Zhong, H. Ding and D. Chen, *Chin. J. Catal.*, 2019, **40**, 446–457.

14 Q. Wang, Q. Gao, H. Wu, Y. Fan, D. Lin, Q. He, Y. Zhang and Y. Cong, *Sep. Purif. Technol.*, 2019, **226**, 232–240.

15 Y.-Q. Ye, G.-H. Gu, X.-T. Wang, T. Ouyang, Y. Chen and Z.-Q. Liu, *Int. J. Hydrogen Energy*, 2019, **44**, 21865–21872.

16 A. Malathi, P. Arunachalam, V. S. Kirankumar, J. Madhavan and A. M. Al-Mayouf, *Opt. Mater.*, 2018, **84**, 227–235.

17 Y. Liu, J. Wei, Y. Liu, X. Bai, P. Shi, S. Mao, X. Zhang, C. Li and B. Dkhil, *J. Mater. Sci.: Mater. Electron.*, 2015, **27**, 3095–3102.

18 T. W. Kim and K. S. Choi, *Science*, 2014, **343**, 990–994.

19 S. K. Singh, H. Ishiwara and K. Maruyama, *Appl. Phys. Lett.*, 2006, **88**, 262908.

20 K.-H. Ye, Z. Chai, J. Gu, X. Yu, C. Zhao, Y. Zhang and W. Mai, *Nano Energy*, 2015, **18**, 222–231.

21 A. Helal, F. A. Harraz, A. A. Ismail, T. M. Sami and I. A. Ibrahim, *Appl. Catal., B*, 2017, **213**, 18–27.

22 A. Malathi, P. Arunachalam, J. Madhavan, A. M. Al-Mayouf and M. A. Ghanem, *Colloids Surf., A*, 2018, **537**, 435–445.

23 T. Liu, Y. Xu, S. Feng and J. Zhao, *J. Am. Ceram. Soc.*, 2011, **94**, 3060–3063.

24 L. Zhang, J. Ran, S.-Z. Qiao and M. Jaroniec, *Chem. Soc. Rev.*, 2019, **48**, 5184–5206.

25 J. Low, J. Yu, M. Jaroniec, S. Wageh and A. A. Al-Ghamdi, *Adv. Mater.*, 2017, **29**, 1–20.

26 L. Yu, Y. Zhang, J. He, H. Zhu, X. Zhou, M. Li, Q. Yang and F. Xu, *J. Alloys Compd.*, 2018, **753**, 601–606.

27 L. Yu, Y. Zhang, Q. Zhi, Q. Wang, F. S. Gittleson, J. Li and A. D. Taylor, *Sens. Actuators, B*, 2015, **211**, 111–115.

28 Y. Zhang, H. Zhu, L. Yu, J. He and C. Huang, *Mater. Res. Express*, 2018, **5**, 045014.

29 L. Li, P. A. Salvador and G. S. Rohrer, *Nanoscale*, 2014, **6**, 24–42.

30 L. Yu, Y. Zhang, J. He, H. Zhu, X. Zhou, M. Li, Q. Yang and F. Xu, *J. Alloys Compd.*, 2018, **753**, 601–606.

31 J. Song, T. L. Kim, J. Lee, S. Y. Cho, J. Cha, S. Y. Jeong, H. An, W. S. Kim, Y.-S. Jung, J. Park, G. Y. Jung, D.-Y. Kim, J. Y. Jo, S. D. Bu, H. W. Jang and S. Lee, *Nano Res.*, 2017, **11**, 642–655.

32 L. Yu, L. Rishan, Y. Zhang, Q. Wang, Q. Zhi and K. Dong, *J. Optoelectron. Adv. Mater.*, 2014, **16**, 519–523.

33 S. Jeong, J. Song and S. Lee, *Appl. Sci.*, 2018, **8**, 1388.

34 Y. Zhang, J. He, Q. Yang, H. Zhu, Q. Wang, Q. Xue and L. Yu, *J. Power Sources*, 2019, **440**, 227120.

35 H. Huang, Y. He, X. Du, P. K. Chu and Y. Zhang, *ACS Sustainable Chem. Eng.*, 2015, **3**, 3262–3273.

36 E. M. Steinmiller and K. S. Choi, *Proc. Natl. Acad. Sci. U. S. A.*, 2009, **106**, 20633–20636.

37 J. Shi, P. Zhao and X. Wang, *Adv. Mater.*, 2013, **25**, 916–921.

38 X. Wu, H. Li, X. Wang, L. Jiang, J. Xi, G. Du and Z. Ji, *J. Alloys Compd.*, 2019, **783**, 643–651.